

Received 30 September 2022; revised 9 November 2022; accepted 15 November 2022. Date of publication 18 November 2022;
date of current version 22 December 2022. The review of this article was arranged by Associate Editor James Morris.

Digital Object Identifier 10.1109/OJNANO.2022.3223151

Copper Passivated Zigzag MgO Nanoribbons for Potential Nanointerconnect Applications

M. SANKUSH KRISHNA¹, SANGEETA SINGH¹ (Member, IEEE), AND BRAJESH KUMAR KAUSHIK² (Senior Member, IEEE)

¹Microelectronics and VLSI lab, National Institute of Technology, Patna 800005, India

²Department of Electronics and Communication Engineering, Indian Institute of Technology Roorkee, Roorkee 247667, India

CORRESPONDING AUTHOR: SANGEETA SINGH (e-mail: sangeeta.singh@nitp.ac.in)

ABSTRACT The present work explores the theoretical analysis of copper passivated MgONRs (Cu-MgO-Cu) for possible nanointerconnect applications. The first principles calculations based on density functional theory (DFT) and non-equilibrium Green's function are employed for theoretical investigation. Pristine MgONRs (H-MgO-H) and Cu-MgO-Cu are both thermodynamically stable and are metallic with H-MgO-H being relatively more stable. Further, the I-V characteristics evaluated using the two-probe method reveal the ohmic behavior of Cu-MgO-Cu. The Cu-MgO-Cu device is further investigated for the nanointerconnect applications. The computed nanoscale parasitic components such as quantum resistance (R_Q), quantum capacitance (C_Q), and kinetic inductance (L_K) are computed to be 6.46 kΩ, 5.57 fF/μm, and 58.17 nF/μm, respectively. Furthermore, the delay and power delay product (PDP) of the nanointerconnect are explored which are important attributes of nanointerconnects. The findings suggest the Cu-MgO-Cu nanoribbons with low parasitic parameters can potentially be employed for nanointerconnect applications.

INDEX TERMS MgO nanoribbons, Density functional theory (DFT), Nano-interconnects, Non-equilibrium Green's function (NEGF).

I. INTRODUCTION

The scaling of present silicon technologies can no longer follow the Moore's law [1]. Various significant physical parameters arise at sub-nano dimensions that start to deteriorate the semiconductor device performance such as short channel effects (SCEs), leakage currents, tunneling effects etc [2]. Hence, the researchers have started to deploy 2D materials as the channel material in the devices [3]. In view of this, the research fraternity has started exploring the 2D materials. 2D materials exhibit peculiar structural and electronic properties [4]. The first synthesis of graphene with a hexagonal honeycomb structure further fueled this research to an even greater extent [5]. However, the inherent limitations of graphene such as intrinsic zero bandgap motivated the researchers to extend their investigations to other 2D materials [6].

At nanoscale dimensions, the designed devices demand nano-interconnects. Conventionally used aluminium (Al) interconnects are replaced by copper (Cu) interconnects [7]. There are significant issues with using Cu as a metal

connection at lower dimensions due to its increased resistivity, grain boundary scattering, and electron migration [8], [9]. Various 2D materials have been reported for use in the design of metal interconnects at the nanoscale [10], [11], [12], [13]. Theoretical research has shown that GNRs can be used for nanoscale interconnects with chemical edge modification [14] or by doping [15]. The very next material in the same group i.e., silicene is investigated for the interconnect design [13], [16]. Later, the following material germanene is functionalized with oxygen for the interconnect design [12]. The germanene nanoribbons (GeNRs) with asymmetric edges are found to induce the linear current behavior with applied bias. A similar phenomenon is previously reported in silicene nanoribbons (SiNRs) with asymmetric edges [17]. Also, other 2D materials such as zigzag arsenene nanoribbons (zAsNRs) and gallium nitride nanoribbons (GaNNRs) are reported for the nanointerconnects design [18], [19].

Metal oxides belong to 2D materials that have been the subject of substantial study due to the potential technical applications they show in areas like electronic and

photonic devices [20], [21]. Considering this, magnesium oxide (MgO) is an intriguing substance with remarkably exceptional optical, electrical, and magnetic characteristics [22]. On a variety of substrates, non-polar and polar 2D MgO are synthesized [23], [24], [25]. A lot of research is being done on 2D polar MgO structures because of their fascinating magnetic and electrical characteristics [26], [27]. Theoretical investigations on polar MgO nanoribbons (MgONRs) have recently been reported [28]. Bare-edged polar MgONRs demonstrate metallic nature. MgONR research is still in its early stages, nevertheless. Many research works proposed the design of field effect transistors (FETs) by using MgO as the gate dielectric material [29]. In our present work we propose the novel application of MgO as a nanointerconnect in electronic applications.

In the present work, zigzag MgONRs are theoretically investigated for possible applications as nanointerconnect. MgONRs are edge passivated with copper atoms to investigate the interconnect applications. The bandstructure calculations reveal the pristine MgONRs (H-MgO-H) and the copper passivated MgONRs (Cu-MgO-Cu) are metallic. The transport characteristics investigations reveal the linear I-V characteristics for the Cu-MgO-Cu signifying their potential as nanointerconnect. Further, the parasitic parameters that affect the interconnecting performance are evaluated along with the delay and power delay product (PDP) analysis.

The following is the outline for this manuscript. The simulated computational method is reported in Section II. Following an in-depth analysis of the acquired simulation findings in Section III, we conclude our discussion in Section IV.

II. COMPUTATIONAL DETAILS

For the current theoretical studies, we employ the DFT calculations coupled with the non-equilibrium Green's function (NEGF) formalism as implemented in the QuantumWise ATK package [30], [31]. The considered MgONR configurations are shown in Fig. 1. The pristine MgONRs are depicted in Fig. 1(a) and the copper passivated nanoribbons are depicted in Fig. 1(b). The unit cell of the nanoribbon to investigate the structural and electronic properties using the supercell approach is shown with dashed rectangular section. The structure comprises of 6 Mg and O atoms each and two passivated atoms. The unit cell of the nanoribbons are periodic in Z-direction and constrained in the X and Y directions. The interference from the periodic replications in X and Y directions is avoided with an enough vacuum spacing of 10 Å. The nanoribbon structures are firstly relaxed to obtain the ground state energy. The ground state energy is said to have been obtained when the coulombic atomic forces between the atoms are less than 0.01 eV with a tolerance limit of 4×10^{-5} [31]. Generalized gradient approximation (GGA) method within the framework of Perdew-Burke-Ernzerhof (PBE) functional is used to consider the exchange correlational effects in the computations [32]. The Brillouin zone is sampled with a dense

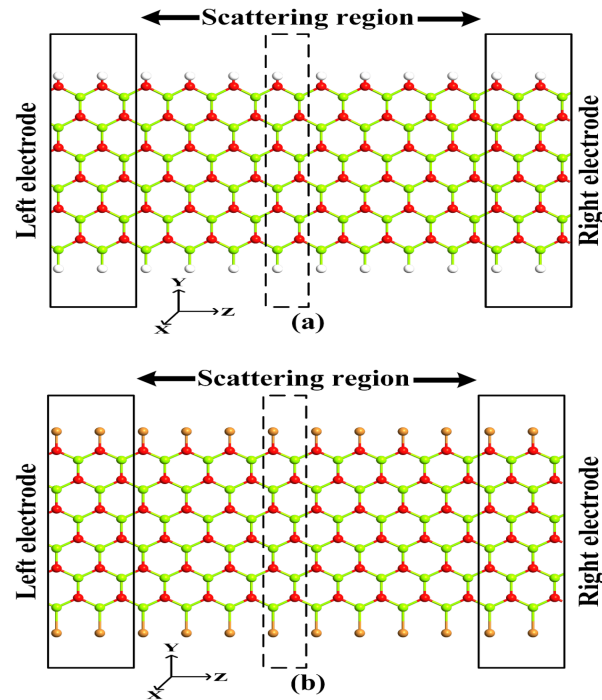


FIGURE 1. Two-terminal device configurations of MgONRs (a) H-MgO-H and (b) Cu-MgO-Cu . The rectangular regions indicate the electrodes and the dashed rectangular section represents the unit cell.

k-point meshing of about $1 \times 1 \times 100$ [21]. A mesh cut-off energy of about 75 Ha is used with double zeta polarized basis set. The stability of the MgONRs are investigated with the binding energy calculations (E_b). The E_b is computed using the expression shown in (1) [33].

$$E_b = \frac{1}{N_T} (E_T - pE_{\text{Mg}} - qE_O - rE_P) \quad (1)$$

The total energy of a single passivated atom, one O atom, one Mg atom, and the whole nanoribbon under consideration are denoted by E_P , E_O , E_{Mg} , and E_T , respectively. Total magnesium atoms, passivated atoms, and oxygen atoms are represented by p , r , and q , respectively. The total number of atoms in the unit cell is indicated by N_T . The study is further extended to investigate the quantum transport characteristics of the MgONRs . NEGF formalism is employed to investigate the transport properties. Two-probe geometry method implemented in ATK is employed for the investigation of transport characteristics. The semi-infinite electrodes with periodic boundary conditions are attached on either side of the central scattering region. The scattering region considered for the study is about eight unit cells in length and electrodes of about two unit cells. The length of the scattering region is 2.632 nm and the electrodes are 0.658 nm, respectively. The transport characteristics of the two-probe device are modeled

using the expressions shown below [33], [34]:

$$I(V) = \frac{2e^2}{h} \int_{\mu_L}^{\mu_R} T(E, V) [F(E - \mu_L) - F(E - \mu_R)] dE \quad (2)$$

where $T(E, V)$ stands for the transmission coefficient, which may be determined by using the relation in (3) and $\mu_{(R/L)}$ indicate the electrochemical potentials of the right/left electrodes, respectively.

$$T(E, V) = T_r[\tau_R(E, V)G_C(E, V)\tau_L(E, V)G_C^+(E, V)] \quad (3)$$

where $G_C(E, V)$ and $G_C^+(E, V)$ are the retarded and advanced Green's function of the scattering region. Here, $\tau_{(L/R)}(E, V)$ represent the coupling coefficients for the left/right contacts. Assessing the retarded Green's function is crucial.

$$G_C(E) = \frac{1}{(E + i\delta_+)S - H} \quad (4)$$

where δ_+ denotes an infinitesimal positive number while the overlap and Hamiltonian matrices of the entire system are represented by S and H , respectively. By simply adding the self-energies of the electrodes to the central region's Hamiltonian, we may obtain the Green's function:

$$G_C(E) = (E + i\delta_+)S - H - [\Sigma^L(E) - \Sigma^R(E)]^{-1} \quad (5)$$

where $\Sigma^{L/R}$ stands for the left/right electrode self-energies. The central-region Hamiltonian matrix must be inverted in order to calculate $G_C(E)$ at a given energy. The latter is represented in a sparse format, thus all we need is the density matrix for same sparsity pattern. Block diagonal inversion method is used for this [35].

III. RESULTS AND DISCUSSION

An in-depth discussion of the obtained simulation results is provided in the current section. For a convenient reading, the section is split into sub-sections such as structural properties, electronic properties, and transport properties.

A. STRUCTURAL PROPERTIES

The structural attributes of the nanoribbon are detailed in the current section. For the H-MgO-H shown in Fig. 1(a), the edge Mg-O bond lengths are measured to be 1.92 Å. The O-H bond length at O-rich edge is measured to be 0.97 Å and Mg-H bond length at Mg-rich edge is measured to be 1.77 Å, respectively. The copper passivated nanoribbons are shown in Fig. 1(b). For the Cu-MgO-Cu, the edge Mg-O bond lengths are reduced to 1.86 Å at O-rich edge and 1.88 Å at the Mg-rich edge, respectively. The Cu-O bond length at O-rich edge and the Cu-Mg bond length at the Mg-rich edge are measured to be 1.83 Å and 2.44 Å, respectively. The higher bond lengths with Cu could be attributed to the higher atomic radius of the Cu atom. The Mg-O bond lengths at the O-rich edge are lower when compared to Mg-rich edge for the Cu-MgO-Cu. The increase in bond length at Mg-rich edge

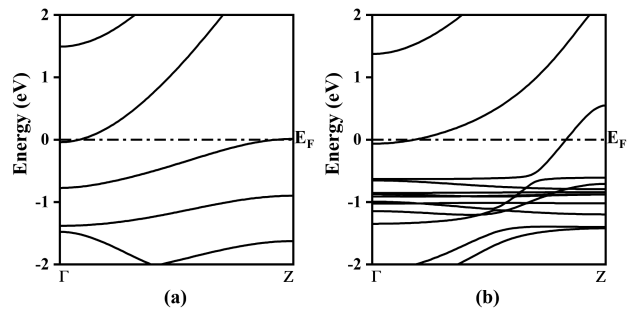


FIGURE 2. Bandstructure plots of the MgONRs (a) H-MgO-H and (b) Cu-MgO-Cu.

could be attributed to the lower charge transfer at Mg-rich edge.

Further, the stability analysis of the nanoribbons is performed based on the E_b calculations. For the H-MgO-H nanoribbon, the E_b is found to be -5.23 eV. The negative E_b indicates the thermodynamic stability of the structure. For the Cu-MgO-Cu the E_b is computed to be -5.08 eV. The E_b is slightly reduced as compared to H-MgO-H. The Cu-MgO-Cu is relatively less stable as compared to H-MgO-H. The decrease in binding energy could be attributed to the higher charge transfer between the edge copper atoms and the host atoms.

B. ELECTRONIC PROPERTIES

To investigate the electronic properties bandstructure and density of states (DOS) computations are performed. The bandstructures of the considered nanoribbons under study are shown in Fig. 2. The dash-dotted line at the center indicates the Fermi energy level (E_F). The E_F is shifted to 0 eV for an easier interpretation of the electronic characteristics. For the pristine MgONR shown in Fig. 2(a), two energy bands cross the E_F . This indicates the metallic nature of the nanoribbons. The energy state in the conduction band is mostly contributed by the edge O atoms and the valence band energy state major contribution is due to the interaction between the edge Mg atoms and the passivated H atoms. Further, the bandstructure plots of the Cu-MgO-Cu is shown in Fig. 2(b). The energy bands crossing the E_F indicate the metallic nature of the device similar to the H-MgO-H nanoribbon structures. The interaction between the Cu and Mg atom induces the conduction band energy state at E_F . The energy state of the valence band is mostly due to copper and oxygen atom interactions at the edge. The energy states in valence band become denser for the Cu-MgO-Cu, which could be due to the passivated Cu atom.

Further, the DOS plots are illustrated in Fig. 3. The dash-dotted line at the center indicates the $E - E_F$ energy level. The non-zero DOS at E_F indicates the availability of energy states at E_F . This is consistent with the metallic nature reported in bandstructure calculations [Fig. 2]. The valence

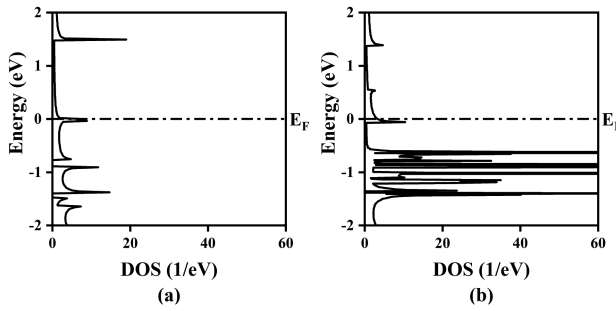


FIGURE 3. DOS plots of the MgONRs (a) H-MgO-H and (b) Cu-MgO-Cu.

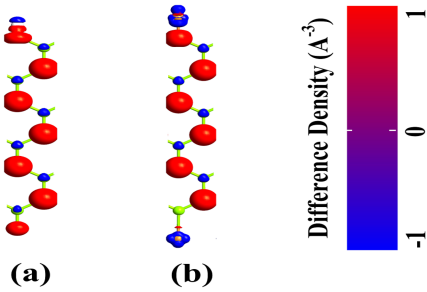


FIGURE 4. The computed charge difference density plots of the MgONRs (a) H-MgO-H and (b) Cu-MgO-Cu.

DOS are mostly due to the Mg-rich edge atoms and the conduction DOS states are mostly due to the O-rich edge atoms. For the Cu-MgO-Cu depicted in Fig. 3(b), the non-zero DOS at E_F is in agreement with metallic nature. The DOS values of the valence band are significantly enhanced when compared with H-MgO-H due to the passivated copper atoms. The interaction between the copper and edge host atoms attribute the non-zero DOS at E_F .

Further, the interaction between the atoms is evaluated with the charge difference density plots. The charge difference plots of the MgONRs is shown in Fig. 4 . For both the nanoribbons, the charge density is positive at the O-atom sites [36]. The gaining of electrons is represented by positive charge density and the loss of electrons is depicted by the negative charge density, respectively. Thus oxygen atoms sites as the charge accumulation sites and Mg-atoms sites demonstrate the charge depletions regions. For the Cu-MgO-Cu, the copper atoms act as the charge depletion regions with negative charge density.

C. TRANSPORT PROPERTIES

The NEGF formalism as implemented in the ATK package is used to investigate the transport characteristics of the MgONR devices. Fig. 1 depicts the two-probe device arrangement of the MgONR devices. The solid rectangular sections on either sides represent the electrode regions. The transmission spectrum at zero bias voltage and the acquired I-V characteristics are depicted in Fig. 5(a) and (b), respectively. Both the H-MgO-H and Cu-MgO-Cu devices feature a non-zero transmission peak at zero energy level at zero bias as illustrated in Fig. 5(a). This means that there are available transmission channels at zero bias which is attributed to their metallic

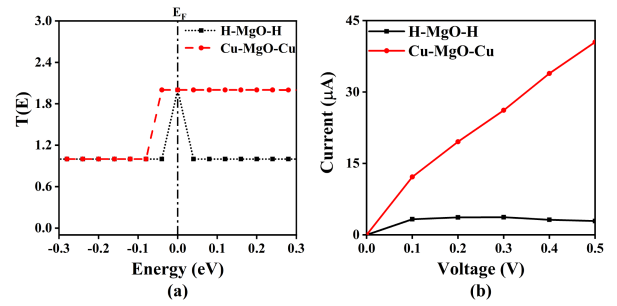


FIGURE 5. The computed (a) zero bias transmission spectrum and (b) I-V characteristics of the MgONRs.

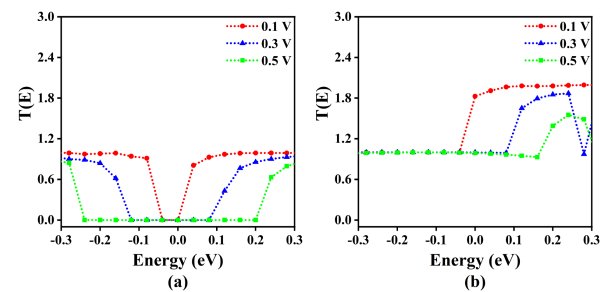


FIGURE 6. The computed transmission spectrum plots at different applied bias voltages for (a) H-MgO-H and (b) Cu-MgO-Cu.

nature. Fig. 5(b) presents the obtained I-V characteristics. Until a value of 0.3 V is reached, the current in an H-MgO-H device rises, and then it begins to decline as the voltage is increased. This indicates the negative differential resistance (NDR) characteristic, where the current drops as the bias is increased [37]. For the copper passivated device, the current increases with applied bias linearly, indicating its potential to be deployed as the nanointerconnect. The current magnitude of the copper passivated device is higher when compared to H-MgO-H device which could be due to the passivated copper atoms. Since the Cu-MgO-Cu exhibits linear I-V behavior it is further investigated for the nanointerconnect performance.

To have an understanding of the I-V characteristics, the bias dependent transmission spectrum plots are depicted in Fig. 6 . For an applied voltage bias V_b , the area under the transmission spectrum curve within the bias energy window $\pm eV_b/2$ determines the magnitude of the current. For the H-MgO-H device shown in Fig. 6(a), the transmission area increases at 0.3 V when compared to 0.1 V. This leads to an increase in current magnitude as reported in Fig. 5(b). At 0.5 V bias voltage, the transmission area within the bias voltage region is slightly reduced which results in reduced magnitude of current. For the Cu-MgO-Cu, the area under the transmission curve within the energy bias window increases consistently with applied bias voltage. This results in linear I-V characteristics which is in good agreement with the results reported in Fig. 5(b). Furthermore, local device DOS (LDOS) is plotted for iso-surface visualization of the energy states. The LDOS plots are shown in Fig. 7. As can be observed from Fig. 7, the DOS distribution is mostly seen at the edges. The transmission of carriers occurs mostly at the edges. The LDOS delocalization

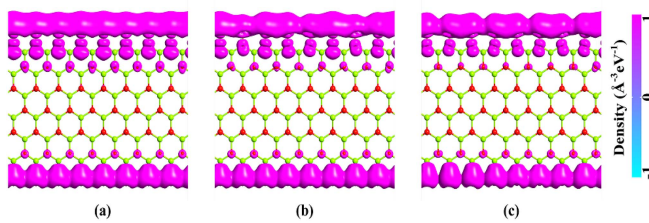


FIGURE 7. Bias dependent LDOS of Cu-MgO-Cu device at (a) 0.1 V (b) 0.3 V, and (c) 0.5 V.

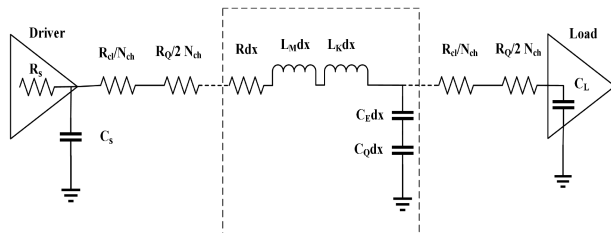


FIGURE 8. Driver-interconnect-load setup of Cu-MgO-Cu nanointerconnect device.

is consistent at edges with applied bias voltage which supports the linear I-V characteristics reported in Fig. 5(b).

D. DYNAMICAL PARAMETER ANALYSIS

At nanometer scales, parasitic parameters significantly affect device performance. Parasitic inductances and capacitances begin to have a notable effect on device performance. In general, the nanoscale interconnects can be modelled with a distributed circuit. Fig. 8 shows a nanoscale representation of the interconnect distributed circuit concept [38]. The dotted rectangular section depicts the distributed network. The dx in the figure represents the very small length. Kinetic/magnetic inductances (L_K/L_M), and quantum/electrostatic capacitance (C_Q/C_E), as seen in the image, all have a substantial effect on interconnect performance. The C_Q and L_K appear due to the exchange correlational effects and are unique to the nanoscale devices [13]. Furthermore, the resistance in the two-probe setup can be evaluated as follows [7]

$$R_Q = \frac{1}{G_Q} = \frac{h}{2q^2 N_{ch}} \quad (6)$$

In (6), R_Q represents the quantum resistance and G_Q represents the quantum conductance. It can be observed that the R_Q is dependent on the number of transmission channels (N_{ch}), charge of electron (q), and Planck's constant (h). So, the transmission eigenvalues/modes (also called transmission channels) are evaluated for the Cu-MgO-Cu device. The N_{ch} of the Cu-MgO-Cu and H-MgO-H device is found to be 2. The evaluated, R_Q of the interconnect is computed to be 6.46 k Ω for both devices. Further, the dynamic parameters are evaluated. The expressions used to model the L_K and C_Q are shown in (7) and (8), respectively.

$$L_K = \frac{h}{4q^2 v_f N_{ch}} \quad (7)$$

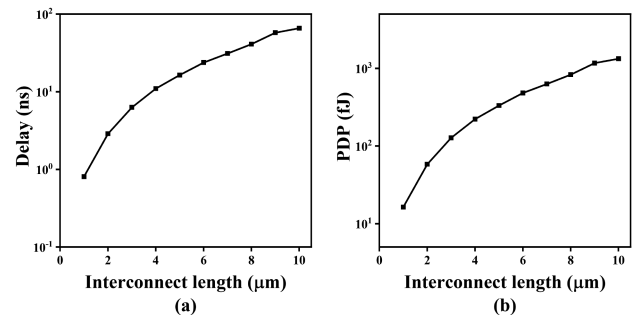


FIGURE 9. The computed (a) Delay and (b) Power delay product of the Cu-MgO-Cu device.

$$C_Q = \frac{4q^2}{hv_f} N_{ch} \quad (8)$$

wherein, v_f represents the Fermi velocity. L_K and C_Q depend on q , N_{ch} , h , and an additional parameter Fermi velocity (v_f). The v_f is evaluated from the $E - K$ relations as follows [12].

$$v_f = \frac{1}{\hbar} \frac{dE}{dk} \quad (9)$$

wherein \hbar represents the reduced Planck's constant.

The v_f of the Cu-MgO-Cu device is computed to be 5.55×10^4 m/s. Further, the L_K and C_Q are computed using the v_f . The computed L_K and C_Q of the Cu-MgO-Cu device are 5.57 fF/ μ m and 57.18 nH/ μ m, respectively. The computed C_Q and L_K values for H-MgO-H are found to be 3.47 fF/ μ m and 3.62 nH/ μ m, respectively.

In an electronic chip the delay mostly occurs due to the nano-interconnects. Hence, the delay of the interconnect system is an important attribute to evaluate its performance. The delay and power delay product (PDP) of the Cu-MgO-Cu are evaluated and depicted in Fig. 9(a) and (b). The delay of the nano-interconnects is evaluated by constructing the interconnect system described in Fig. 8. The simulations are performed in the LTspice simulation tool. As can be observed from Fig. 9(a), the delay of the interconnect increases with an increase in interconnect length. Further, the PDP is evaluated by taking the product of the computed power consumption and the delay of the circuit. The power consumption in the circuit is evaluated using the expression shown in (10). For the best performing interconnect, the delay and the PDP need to be as low as possible.

$$P = I \times V_{max} \quad (10)$$

wherein, V_{max} corresponds to the maximum applied voltage i.e., 0.5 V and I represents the corresponding current magnitude at V_{max} . The evaluated PDP with interconnect length is depicted in Fig. 9(b). As the interconnect length is increased the PDP is increased due to increased delay.

A brief comparison of the obtained findings with the reported interconnect literature is presented in Table 1. Table 2 illustrates the merits of MgO over other materials. Though, germanene nanoribbon (GeNR), silicene nanoribbon (SiNR), and arsenene nanoribbon (AsNR) have better v_f compared to Cu-MgO-Cu, MgO has unique attributes such as simple

TABLE 1. Extracted Parameters of Selective Edge Passivated Nano-Interconnects

Structure	Orientation	v_f (m/s)	R_Q (kΩ)	C_Q (fF/μm)	L_K (nH/μm)	Ref.
F-ZGNR-F	Planar	4.74×10^4	4.3	9.8	45.37	[14]
SiNR	Buckled	7.28×10^4	NR	2.12	88.7	[13]
GeNR	Buckled	9.89×10^4	NR	1.57	65.3	[13]
C-ZGeNR-O	Buckled	4.88×10^5	6.25	1.26	3.32	[15]
O-ZGeNR-O	Buckled	5.21×10^5	NR	0.889	4.14	[12]
zAsNR	Buckled	3.16×10^5	NR	0.98	10.2	[18]
Cu	Square	2.37×10^4	2.58	32.60	54.6	[39]
Cu-MgO-Cu	Planar	5.55×10^4	6.46	5.57	57.18	—

*NR: Not reported

TABLE 2. Extracted Parameters of Selective Edge Passivated Nano-Interconnects

Structure	Melting point (K) [Ref]	Thermal conductivity(W/m-K) [Ref]
Graphene	4510 [40]	4000 [41]
Silicene	1500 [42]	50 [43]
Germanene	1710 [44]	60 [45]
Arsenene	230 [46]	30.4 [47]
Copper	910 [48]	400 [49]
MgO	3125 [50]	30 [51]

*NR: Not reported

stoichiometry, structural planarity, high melting point, and low thermal conductivity. In addition to the ease of synthesis, its remarkable electronic, magnetic, and optical properties make them the most favored structures over other materials [23]. MgONRs can further be explored for even better characteristics to employ in nano-electronics.

IV. CONCLUSION

In summary, the first principles investigation of copper passivated MgONRs for possible interconnect applications is explored. DFT investigations with NEGF formalism are deployed for theoretical computations. Binding energy calculations reveal that both H-MgO-H and Cu-MgO-Cu are thermodynamically stable with H-MgO-H being most stable of the two. Bandstructure calculations reveal metallic nature for both structures. The copper atoms dominate the metallic nature in Cu-MgO-Cu. The two-probe method is further used to investigate the transport characteristics. The I-V computations reveal the linear behavior of Cu-MgO-Cu device which is further investigated for interconnect performance. The dynamic parameters that affect the interconnect performance such R_Q , C_Q , and L_K are evaluated to be 6.46 kΩ, 5.57 fF/μm, and 58.17 nH/μm, respectively. Also, the delay and PDP of the interconnect distributed circuit model is evaluated and found to increase with an increase in interconnect length. Based on the obtained findings the MgONRs can be employed as nanointerconnect due to their peculiar merits such as structural planarity, high melting point, exciton binding energy, low thermal conductivity, and ease of synthesis.

REFERENCES

- [1] T. Radsar, H. Khalesi, and V. Ghods, “Graphene nanoribbon field effect transistors analysis and applications,” *Superlattices Microstruct.*, vol. 153, 2021, Art. no. 106869.
- [2] R. Ratnesh, A. Goel, G. Kaushik, H. Garg, M. Singh, and B. Prasad, “Advancement and challenges in MOSFET scaling,” *Mater. Sci. Semicond. Process.*, vol. 134, 2021, Art. no. 106002.
- [3] K. Khan et al., “Recent developments in emerging two-dimensional materials and their applications,” *J. Mater. Chem. C*, vol. 8, no. 2, pp. 387–440, 2020.
- [4] R. Mas-Balleste, C. Gomez-Navarro, J. Gomez-Herrero, and F. Zamora, “2D materials: To graphene and beyond,” *Nanoscale*, vol. 3, no. 1, pp. 20–30, 2011.
- [5] K. S. Novoselov et al., “Electric field effect in atomically thin carbon films,” *Science*, vol. 306, no. 5696, pp. 666–669, 2004.
- [6] J. M. Marmolejo-Tejada and J. Velasco-Medina, “Review on graphene nanoribbon devices for logic applications,” *Microelectron. Eng.*, vol. 48, pp. 18–38, 2016.
- [7] S. Agrawal, A. Srivastava, G. Kaushal, and A. Srivastava, “Edge engineered graphene nanoribbons as nanoscale interconnect: DFT analysis,” *IEEE Trans. Nanotechnol.*, vol. 21, pp. 43–51, 2022.
- [8] W. Steinhögl, G. Schindler, G. Steinlesberger, M. Traving, and M. Engelhardt, “Comprehensive study of the resistivity of copper wires with lateral dimensions of 100 nm and smaller,” *J. Appl. Phys.*, vol. 97, no. 2, Art. no. 023706.
- [9] K.-H. Koo, P. Kapur, and K. C. Saraswat, “Compact performance models and comparisons for gigascale on-chip global interconnect technologies,” *IEEE Trans. Electron Devices*, vol. 56, no. 9, pp. 1787–1798, Sep. 2009.
- [10] F. Kreupl et al., “Carbon nanotubes in interconnect applications,” *Microelectron. Eng.*, vol. 64, no. 1–4, pp. 399–408, 2002.
- [11] A. Smolyanitsky and V. Tewary, “Atomistic simulation of a grapheme-nanoribbon–metal interconnect,” *J. Phys. Condens. Matter*, vol. 23, no. 35, 2011, Art. no. 355006.
- [12] V. Sharma, P. Srivastava, and N. K. Jaiswal, “Edge-oxidized germanene nanoribbons for nanoscale metal interconnect applications,” *IEEE Trans. Electron Devices*, vol. 65, no. 9, pp. 3893–3900, Sep. 2018.
- [13] S. Yamacli, “Investigation and comparison of the large-signal characteristics and dynamical parameters of silicene and germanene nanoribbon interconnects,” *Comput. Mater. Sci.*, vol. 141, pp. 353–359, 2018.
- [14] M. Jatkar, K. K. Jha, and S. K. Patra, “First-principles investigation of f-functionalized ZGNR/AGNR for nanoscale interconnect applications,” *J. Comput. Electron.*, vol. 20, no. 4, pp. 1461–1470, 2021.
- [15] V. Sharma and P. Srivastava, “Probing gold-doped germanene nanoribbons for nanoscale interconnects under DFT-NEGF framework,” *J. Electron. Mater.*, vol. 49, no. 6, pp. 3938–3946, 2020.
- [16] S. Yamacli, “Comparison of the electronic transport properties of metallic graphene and silicene nanoribbons,” *J. Nanopart. Res.*, vol. 16, no. 8, pp. 1–9, 2014.
- [17] J. Kang, F. Wu, and J. Li, “Symmetry-dependent transport properties and magnetoresistance in zigzag silicene nanoribbons,” *Appl. Phys. Lett.*, vol. 100, no. 23, 2012, Art. no. 233122.
- [18] S. Yamacli, “Investigation of static and dynamic electronic transport characteristics of zigzag arsenene nanoribbons: An ab-initio study,” *Mater. Today Commun.*, vol. 25, 2020, Art. no. 101581.
- [19] M. Jatkar, K. K. Jha, and S. K. Patra, “Fe-functionalized zigzag GaN nanoribbon for nanoscale spintronic/interconnect applications,” *Appl. Phys. A*, vol. 127, no. 6, pp. 1–10, 2021.
- [20] J. Beheshtian, A. Ahmadi Peyghan, and Z. Bagheri, “Ab initio study of NH₃ and H₂O adsorption on pristine and Na-doped MgO nanotubes,” *Struct. Chem.*, vol. 24, no. 1, pp. 165–170, 2013.
- [21] M. S. Krishna and S. Singh, “Disconnected N-doped zigzag ZnO nanoribbon for potential negative differential resistance (NDR) applications,” *Microelectron. J.*, vol. 115, 2021, Art. no. 105204.
- [22] A. Akhtar, R. Pilevarshahi, and M. R. Benam, “Investigating and comparison of electronic and optical properties of MgO nanosheet in (100) and (111) structural directions based on the density functional theory,” *Phys. B: Condens. Matter*, vol. 502, pp. 61–67, 2016.
- [23] S. Sagadevan et al., “Effect of synthesis temperature on the morphologies, optical and electrical properties of MgO nanostructures,” *J. Nanosci. Nanotechnol.*, vol. 20, no. 4, pp. 2488–2494, 2020.
- [24] M. Kiguchi, S. Entani, K. Saiki, T. Goto, and A. Koma, “Atomic and electronic structure of an unreconstructed polar MgO (111) thin film on Ag (111),” *Phys. Rev. B*, vol. 68, no. 11, 2003, Art. no. 115402.
- [25] K. Matsuzaki, H. Hosono, and T. Susaki, “Layer-by-layer epitaxial growth of polar MgO (111) thin films,” *Phys. Rev. B*, vol. 82, no. 3, 2010, Art. no. 033408.

- [26] R. Arita, Y. Tanida, S. Entani, M. Kiguchi, K. Saiki, and H. Aoki, "Polar surface engineering in ultrathin MgO (111)/ Ag (111): Possibility of a metal-insulator transition and magnetism," *Phys. Rev. B*, vol. 69, no. 23, 2004, Art. no. 235423.
- [27] P. Wu, M. Huang, W. Cheng, and F. Tang, "First-principles study of B, C, N and F doped graphene-like MgO monolayer," *Physica E: Low Dimens. Syst. Nanostructures*, vol. 81, pp. 7–13, 2016.
- [28] J. Goniakowski, L. Giordano, and C. Noguera, "Polarity compensation in low-dimensional oxide nanostructures: The case of metal-supported MgO nanoribbons," *Phys. Rev. B*, vol. 87, no. 3, 2013, Art. no. 035405.
- [29] P. Karmakar and P. Sahu, "Modified gate oxide double gate tunnel field-effect transistor," *Silicon*, vol. 14, no. 12, pp. 6729–6736, 2022.
- [30] M. Brandbyge, J.-L. Mozos, P. Ordejón, J. Taylor, and K. Stokbro, "Density-functional method for nonequilibrium electron transport," *Phys. Rev. B*, vol. 65, no. 16, 2002, Art. no. 165401.
- [31] M. S. Krishna, S. Singh, S. Kharwar, and A. Srivastava, "Nitrogen doped armchair ZnO nanoribbons for potential rectification applications: DFT analysis," *Superlattices Microstruct.*, vol. 159, 2021, Art. no. 107051.
- [32] J. P. Perdew, K. Burke, and M. Ernzerhof, "Generalized gradient approximation made simple," *Phys. Rev. Lett.*, vol. 77, no. 18, 1996, Art. no. 3865.
- [33] S. Kharwar, S. Singh, and N. K. Jaiswal, "First-principles investigations of N-vacancy induced zigzag boron nitride nanoribbons for nanoscale resonant tunneling applications," *J. Electron. Mater.*, vol. 50, no. 10, pp. 5664–5681, 2021.
- [34] M. S. Krishna and S. Singh, "Detection of carcinogenic heavy metals using ZnO nanoribbons (ZnONRs): Ab-initio analysis," *Physica E: Low Dimens. Syst. Nanostructures*, vol. 142, 2022, Art. no. 115289.
- [35] S. Smidstrup et al., "QuantumATK: An integrated platform of electronic and atomic-scale modelling tools," *J. Phys.: Condens. Matter*, vol. 32, no. 1, 2019, Art. no. 015901.
- [36] M. S. Krishna, S. Singh, and M. K. Mohammed, "Carcinogenic heavy metals detection based on ZnO nanoribbons," *IEEE Sensors J.*, vol. 22, no. 17, pp. 16929–16937, Sep. 2022.
- [37] M. S. Krishna and S. Singh, "Fluorinated zigzag ZnO nanoribbons for negative differential resistance-based nanoelectronic devices: First-principles investigation," *J. Electron. Mater.*, vol. 51, no. 6, pp. 3288–3298, 2022.
- [38] V. K. Nishad, A. K. Nishad, B. K. Kaushik, and R. Sharma, "First-principle analysis of transition metal edge-passivated armchair graphene nanoribbons for nanoscale interconnects," *IEEE Trans. Nanotechnol.*, vol. 20, pp. 92–98, 2021.
- [39] S. Agrawala, A. Srivastavaa, and G. Kaushalb, "DFT analysis of different shaped Cu nanowires for interconnect application," in *Proc. 6th Int. Conf. Inf. Technol. High- Perform. Comput.*, 2021, pp. 70–78.
- [40] E. Ganz, A. B. Ganz, L.-M. Yang, and M. Dorfmfeld, "The initial stages of melting of graphene between 4000 K and 6000 K," *Phys. Chem. Chem. Phys.*, vol. 19, no. 5, pp. 3756–3762, 2017.
- [41] M. Hu, X. Zhang, and D. Poulikakos, "Anomalous thermal response of silicene to uniaxial stretching," *Phys. Rev. B*, vol. 87, no. 19, 2013, Art. no. 195417.
- [42] T. K. Min, T. L. Yoon, and T. L. Lim, "Molecular dynamics simulation of melting of silicene," *Mater. Res. Exp.*, vol. 5, no. 6, 2018, Art. no. 065054.
- [43] J. Zhou, H. Li, H.-K. Tang, L. Shao, K. Han, and X. Shen, "Phonon thermal transport in silicene/graphene heterobilayer nanostructures: Effect of interlayer interactions," *ACS Omega*, vol. 7, no. 7, pp. 5844–5852, 2022.
- [44] N. H. Giang, V. Van Hoang, and T. T. T. Hanh, "Melting of two-dimensional perfect crystalline and polycrystalline germanene," *Physica E: Low-Dimensional Syst. Nanostructures*, vol. 119, 2020, Art. no. 114021.
- [45] M. A. Balatero, G. J. Paylaga, N. T. Paylaga, and R. V. Bantaculo, "Molecular dynamics simulations of thermal conductivity of germanene nanoribbons (GeNR) with armchair and zigzag chirality," in *Applied Mechanics and Materials*, vol. 772. Zurich, Switzerland: Trans. Tech. Publ., 2015, pp. 67–71.
- [46] D. Guo, B. Shao, C. Li, and Y. Ma, "Theoretical insight into structure stability, elastic property and carrier mobility of monolayer arsenene under biaxial strains," *Superlattices Microstruct.*, vol. 100, pp. 324–334, 2016.
- [47] M. Zeraati, S. M. V. Allaei, I. A. Sarsari, M. Pourfath, and D. Donadio, "Highly anisotropic thermal conductivity of arsenene: An *ab initio* study," *Phys. Rev. B*, vol. 93, no. 8, 2016, Art. no. 085424.
- [48] L. Somlyai-Sipos, D. Janovszky, A. Sycheva, and P. Baumli, "Investigation of the melting point depression of copper nanoparticles," in *Proc. IOP Conf. Ser.: Mater. Sci. Eng.*, vol. 903, no. 1, 2020, Art. no. 012002.
- [49] S. Bhanushali, N. N. Jason, P. Ghosh, A. Ganesh, G. P. Simon, and W. Cheng, "Enhanced thermal conductivity of copper nanofluids: The effect of filler geometry," *ACS Appl. Mater. Interfaces*, vol. 9, no. 22, pp. 18925–18 935, 2017.
- [50] C. Ronchi and M. Sheindlin, "Melting point of MgO," *J. Appl. Phys.*, vol. 90, no. 7, pp. 3325–3331, 2001.
- [51] A. J. Slifka, B. J. Filla, and J. Phelps, "Thermal conductivity of magnesium oxide from absolute, steady-state measurements," *J. Res. Natl. Inst. Standards Technol.*, vol. 103, no. 4, 1998, Art. no. 357.